MAGNETOHYDRODYNAMICS Vol. 51 (2015), No. 3, pp. 519–530

ANALYTICAL STUDY OF THERMOACOUSTIC MHD GENERATOR

S.M.H. Mirhoseini[1], *A. Alemany*[2]

[1] *KU Leuven, Department of Electrical Engineering (ESAT), Division ELECTA, Kasteelpark Arenberg 10, 3001 Leuven-Heverlee, Belgium*
[2] *Universite Joseph Fourier, SIMAP, 1130 Rue de la Piscine, Grenoble, France*

This paper focuses on an analytical approach to study a cylindrical MHD generator that uses a thermoacoustic engine to apply pressure oscillations of the liquid metal. The fluid motion will induced an electric current in the liquid under the effect of a perpendicular steady magnetic field. The current will be extracted from the MHD channel by induction into a coil surrounding the channel. Few approximations are taken into account in the model, which is based on the Navier–Stokes and induction equations.

Introduction. Electricity production using thermal energy as a primary source is of major importance in industries. Thermoacoustic engines have the potential to produce mechanical energy by velocity vibration when coupled to magnetohydrodynamic (MHD) transducers and are able to generate electricity. The MHD generator is based on the interaction of a DC magnetic field with an oscillating conducting fluid flow to produce AC magnetic fields and current inside the MHD channel. The induced AC magnetic field itself generates an AC electric current in a coil connected to the load by the law of induction [1, 2, 12, 13]. In MHD induction machines, the electric current is produced with an adjustable strength and voltage and does not require any electrodes [3, 14]. A scheme of the thermoacoustic MHD system is demonstrated in Fig. 1, where the MHD generator is submitted to an oscillatory pressure forces.

Neuringer in [4] has analytically studied the MHD generator and focuses on the extraction of optimum power from the steady one-dimensional flow of an incompressible inviscid fluid across a uniform transverse magnetic field in an externally loaded channel of arbitrarily varying cross-section. This investigation has been numerically validated by Aithal [5]. An analytical study on a solar heat coupled MHD generator has been done by Satyamurthy [6]. In that work, a steady-state two-fluid model was used to determine various dynamic parameters of the MHD generator. Different experimental investigations of the MHD generator considering the dynamic behavior and the effect of various MHD non-dimensional parameters on the velocity and induced magnetic field of the generator are pre-

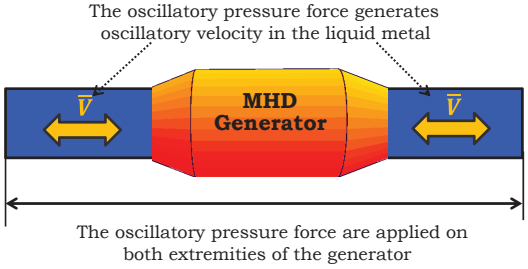

Fig. 1. Scheme of the thermoacoustic MHD generator.

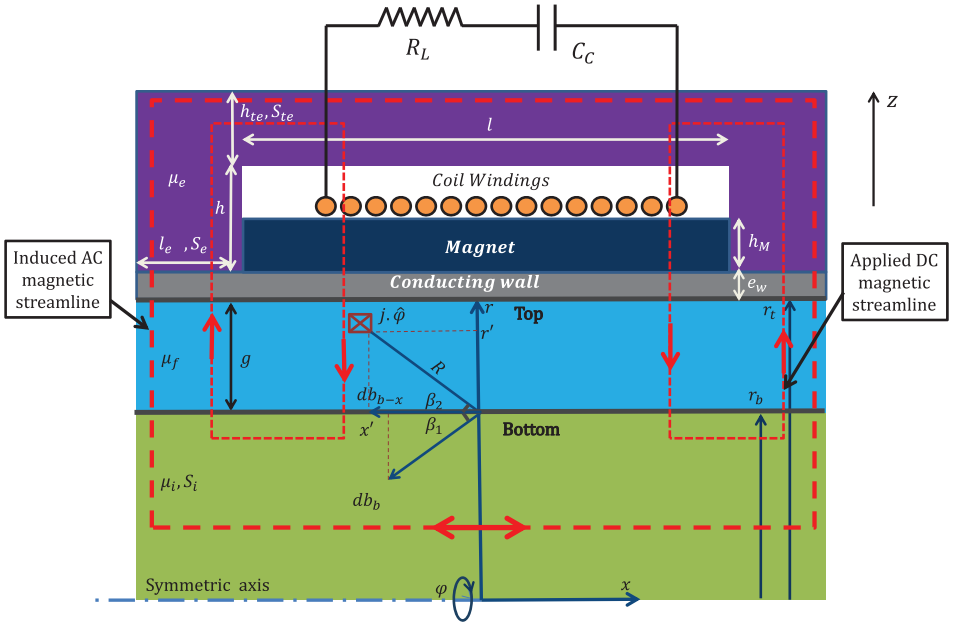

Fig. 2. Scheme of the analytical model of the MHD generator containing a core, an MHD channel, a ferromagnetic yoke, a magnet, an induction coil, load resistance R_{L} and a compensation capacitor C_{C}.

sented in the works by Fabris [7], Dixit [8], Jousselin *et al.* [9] and Marty *et al.* [10].

This paper presents the results of the investigation on the MHD channel characterization with a given oscillatory pressure and velocity applied by the thermoacoustic engine. Due to this oscillating pressure difference, the liquid metal oscillates along the cylindrical MHD channel. A radial magnetic field is produced by a permanent magnet placed around the channel. The interaction between this magnetic field and the liquid motion induces an electric current in the fluid. This AC electric current itself induces a magnetic field interacting with the coil placed externally to the permanent magnet, producing electricity when the load circuit is closed.

1. Description of the model. The analytical model of the system is based on the scheme displayed in Fig. 2. The figure scales are not realistic. The active part of the generator with the length l is supposed to be much larger than the MHD channel depth g, so that it could be considered as infinitely long. The MHD channel contains a liquid metal with the density ρ, dynamic viscosity μ, relative magnetic permeability μ_{f} and electrical conductivity σ_{f}.

The oscillatory pressure gradient applied by the thermoacoustic engine with the amplitude $\nabla p/l$ causes a velocity field with the value $u_0\hat{\mathbf{x}}$ and a pulsation ω in the liquid metal. This velocity field is radially affected by a steady magnetic field $\overline{B} = -B_0\hat{\mathbf{r}}$. The interaction will result in an induced current $j\hat{\boldsymbol{\phi}}$, inducing an AC magnetic field in the ferromagnetic core of the generator. So the generated magnetic flux induces an AC electric current in the external coil connected to the load. Constant and induced magnetic flux lines are shown in Fig. 2.

The magnetic flux closes its path through the core and yoke with the relative permeability μ_{i} and μ_{e}, respectively. The coil that has N turns and an internal resistance r_{C} is connected in series to the load circuit, including a correction capacitor C_{c} and a resistive load R_{L}. The effect of the conducting wall of depth e_{w}

and electrical conductivity $\sigma_{\rm w}$ on the power loss of the generator is also taken into account. The main notations used in this paper are listed in Table 1.

This investigation includes an exact solution of the time dependent induced magnetic field and the true velocity profile of the oscillating liquid metal. Perturbations in fluid velocity produce also a perturbation in induced current, especially in the vicinity of the walls of the liquid metal channel.

2. Problem formulation. The governing equations are based on the following two sets:
a) the Navier-Stokes equation which relates the velocity and pressure with the Lorentz force:

$$\frac{\mathrm{d}\mathbf{V}}{\mathrm{d}t} = -\frac{1}{\rho}\nabla(p' + \rho g_0 z) + \nu\nabla^2\mathbf{V} + \frac{1}{\rho}\mathbf{j}\times\mathbf{B} = -\frac{1}{\rho}\nabla p + \nu.\nabla^2\mathbf{V} + \frac{1}{\rho}\mathbf{j}\times\mathbf{B}; \quad (1)$$

b) the induction equation which is a combination of the Maxwell equations and the Ohm's law:

$$\frac{\partial\mathbf{B}}{\partial t} = \nabla\times\mathbf{V}\times\mathbf{B} - \frac{1}{\mu_0\sigma_{\rm f}}\nabla^2\mathbf{B}, \quad (2)$$

where the total magnetic field $\mathbf{B} = B_0\hat{\mathbf{r}} + b\hat{\mathbf{x}}$ is the contribution of the imposed steady magnetic field and of the induced field, $\mathbf{V}$ is the liquid metal velocity, ρ is the fluid density, p' denotes the oscillatory pressure, $\rho g_0 z$ is the gravitational pressure, ∇p is the total pressure gradient imposed by the thermoacoustic engine, $\nu = \mu/\rho$ is the kinematic viscosity, j is the current density in the liquid, μ_0 stands for the magnetic permeability of the free space.

By assuming that the main variables are of the following form

$$\begin{cases} \mathbf{u} = \Re\mathrm{e}\left\{u\mathrm{e}^{i\omega t}\right\}\hat{\mathbf{x}} \\ \mathbf{B} = B_0\hat{\mathbf{r}} + \Re\mathrm{e}\left\{b_x\mathrm{e}^{i\omega t}\right\}\hat{\mathbf{x}} \\ p = p_0 + \Re\mathrm{e}\left\{(\Delta p/L_{\rm B})x\mathrm{e}^{i\omega t}\right\} \\ \quad\cdots \end{cases} \quad (3)$$

and taking into account the hypothesis of long channel aspect ($l \gg g$), which implies $\mathrm{d}/\mathrm{d}x \ll 1$, and the symmetry in the azimuthal direction, we have:

$$\frac{\partial}{\partial\phi}, \frac{\partial}{\partial x} \approx 0. \quad (4)$$

The current density in the fluid could be calculated by the Ohm's law

$$\mathbf{j} = \sigma_{\rm f}(\mathbf{E} + \mathbf{V}\times\mathbf{B}), \quad (5)$$

where E is the electric field. Assuming the velocity and the imposed field only in one direction will result in

$$\mathbf{V}\times\mathbf{B} = \begin{bmatrix} \hat{\mathbf{r}} & \hat{\boldsymbol{\phi}} & \hat{\mathbf{x}} \\ 0 & 0 & u(r) \\ B_0 & 0 & b_x \end{bmatrix} = B_0 u(r)\hat{\boldsymbol{\phi}}. \quad (6)$$

Then the induced current is

$$\mathbf{j} = \begin{bmatrix} j_r = \sigma_{\rm f}E_r \\ j_\phi = \sigma_{\rm f}\left(E_\phi + B_0 u(r)\right) \\ j_x = \sigma_{\rm f}E_x. \end{bmatrix} \quad (7)$$

Table 1. Main notations used to characterizes the MHD generator.

Scales	Explanation
r_{b}	inner radius of the MHD channel
r_{t}	outer radius of the MHD channel
g	channel gap
e_{w}	wall thickness
h_{M}	magnet thickness
h	inner height of the yoke
h_{te}	thickness of the yoke
L_{B}	length of the active part
l_{e}	length of the yoke pole
S_{i}	cross-section of the core
S_{te}	cross-section of the yoke
S_{e}	cross-section of the yoke leg

Table 2. Non-dimentional scales.

Characteristic scales	Value
Length	g
Magnetic field	B_0
Time	$1/\omega$
Velocity	ωg
Current density	$B_0/\mu_0 g$
Current	$B_0 g/\mu_0$
Electric field	$B_0 g\omega$
Electrical resistance	$1/\sigma g$
Electrical power	${B_0}^2 g/{\mu_0}^2\sigma$

Under the hypothesis $\mathrm{d}/\mathrm{d}x{=}0$ and $\mathrm{d}/\mathrm{d}\phi{=}0$, the continuity equation of the electric current ($\nabla \cdot \mathbf{j} = 0$) implies $\mathrm{d}\mathbf{E}/\mathrm{d}r{=}0$. Because j_r vanishes at the bottom wall of the channel which is insulated, $E_r = 0$ everywhere. If it is assumed to have no applied electric field E_x along the MHD channel, the electric field and, hence, the induced current have only an azimuthal component and the induced magnetic field has the flow direction, as it is expected in Eqs. (3). Then

$$\mathbf{E} = \begin{bmatrix} E_r = 0 \\ E_\phi = E_\phi(r) \\ E_x = 0 \end{bmatrix} \qquad \mathbf{J} = \begin{bmatrix} j_r = 0 \\ j_\phi = j_\phi(r) \\ j_x = 0 \end{bmatrix} \qquad \mathbf{b} = \begin{bmatrix} 0 \\ 0 \\ b_x \end{bmatrix} \tag{8}$$

2.1. Dimensionless equations. The main typical scales used to derive the dimensionless equations are given in Table 2.

Since the depth of the channel is assumed to be several times smaller than the radius of the channel ($g \ll r_{\mathrm{t}}, r_{\mathrm{b}}$), the variations of the channel radius are neglected in the differential equation and the mean value of the channel radius is applied to the model:

$$r = r_{\mathrm{ch}} = \frac{r_{\mathrm{b}} + r_{\mathrm{t}}}{2}. \tag{9}$$

Then the non-dimensional system of differential equations is derived as fol-

Table 3. Characteristic non-dimensional MHD constants.

Symbol	Value	MHD constant	Explanation
Rm	$\mu_{\mathrm{f}}\sigma\omega g^2$	magnetic Reynolds number	ratio of characteristic time of magnetic field diffusion to characteristic time of magnetic field convection
Re_ω	$\rho\omega g^2/\mu$	classical Reynolds number	ratio of inertia forces to viscous forces
N	$B_0^2\sigma/\omega\rho$	interaction parameter	ratio of electromagnetic forces to inertia forces
Ha	$B_0 g\sqrt{\sigma/\mu}$	Hartmann number	ratio of electromagnetic forces to viscous forces
K_{p}	$\dfrac{\nabla p}{L_B\omega^2\rho g}$	pressure constant	dimensionless imposed pressure

lows:

$$\begin{cases} iu^* = -K_{\mathrm{p}} + \dfrac{1}{\mathrm{Re}_\omega}\dfrac{\partial^2 u^*}{\partial r^{*2}} + \dfrac{1}{r_{\mathrm{ch}}\mathrm{Re}_\omega}\dfrac{\partial u^*}{\partial r^*} + \dfrac{N}{\mathrm{Rm}}\dfrac{\partial b^*}{\partial r^*}, \\ ib_x^* = \dfrac{1}{r_{\mathrm{ch}}}u^* + \dfrac{\partial u^*}{\partial r^*} + \dfrac{1}{r_{\mathrm{ch}}\mathrm{Rm}}\dfrac{\partial b_x^*}{\partial r^*} + \dfrac{1}{\mathrm{Rm}}\dfrac{\partial^2 b_x^*}{\partial r^{*2}}. \end{cases} \tag{10}$$

The index <*> indicates the non-dimensional variables. The equations exhibit the non-dimensional parameters listed in Table 3 which control the flow [3, 11].

2.2. Boundary conditions. The system of differential equations (10) needs four boundary conditions to solve the system. From the hydrodynamics point of view, two of these conditions are defined simply by the no-slip wall constrains:

$$u^*(r^* = r_{\mathrm{b}}^*) = 0 \quad u^*(r^* = r_{\mathrm{t}}^*) = 0. \tag{11}$$

The magnetic boundary condition includes the dimensionless induced magnetic flux density at the bottom $b_{x\mathrm{b}}^*$ and at the top $b_{x\mathrm{t}}^*$ of the MHD channel. The induced field at the bottom of the channel in the x-direction is a summation of the following three magnetic sources:

- $b_{x\mathrm{f}}^*$ = magnetic flux density due to induced current inside the liquid
- $b_{x\mathrm{w}}^*$ = magnetic flux density due to induced current inside the wall
- $b_{x\mathrm{L}}^*$ = magnetic flux density due to current in the load.

The induced magnetic field due to the induced current elements inside the liquid is such as

$$\mathrm{d}b_{\mathrm{f}}^* = \frac{g}{2\pi R}B_0^* j^*(r'^*)\mathrm{d}x'^*\mathrm{d}r'^*\mathrm{d}b^*, \tag{12}$$

$$\mathrm{d}b_{x\mathrm{f}}^* = x\sin(\beta_2)\mathrm{d}b_{\mathrm{f}}^*, \tag{13}$$

and $b_{x\mathrm{f}}$ is then calculated by an integration of the elements of the induced field over the cross-section of the channel:

$$b_{x\mathrm{f}}^* = \int_{-l^*/2}^{l^*/2}\int_{r_{\mathrm{b}}^*}^{r_{\mathrm{t}}^*}\frac{r'^* j^*(r'^*)\mathrm{d}x'^*\mathrm{d}r'^*}{2\pi((r^* - r'^*)^2) + (x^* - x'^*)^2}. \tag{14}$$

Assuming the large radius compared to the depth of the MHD channel (i.e. $g^* \ll r_{\mathrm{b}}^*, r_{\mathrm{t}}^*$), the following approximation is applied:

$$|R^*|^2 = (r^* - r'^*)^2 + (x^* - x'^*)^2 \cong g'^{*2} + r'^{*2}. \tag{15}$$

Then $b_{x\mathrm{f}}$ is calculated as

$$b_{x\mathrm{f}}^* = \frac{1}{2\pi}\left(2\tan^{-1}\left(\frac{L_B}{2g}\right)\right)\int_{r_{\mathrm{b}}^*}^{r_{\mathrm{t}}^*} r'^* j^*(r'^*)\mathrm{d}r'^*, \tag{16}$$

where g/L_{B} is the aspect ratio. Secondly, the magnetic field at the bottom of the channel due to the induced current in the wall is determined. The current density in the wall defined by the Ohm's law in the vicinity of the top of the channel takes into account the continuity of the electric field in the liquid and in the wall:

$$\begin{cases} \mathbf{j}_{\mathrm{w}}^* = \left(\dfrac{\sigma_{\mathrm{w}}}{\sigma_{\mathrm{f}}}\right)\mu_{\mathrm{f}}\sigma_{\mathrm{f}}g^2\omega\mathbf{E}_{\mathrm{t}}^* = \left(\dfrac{\sigma_{\mathrm{w}}}{\sigma_{\mathrm{f}}}\right)\mathrm{Rm}\mathbf{E}_{\mathrm{t}}^* \\ \mathbf{E}_{\mathrm{t}}^* = \dfrac{1}{\mathrm{Rm}}\left(\dfrac{\sigma_{\mathrm{f}}}{\sigma_{\mathrm{w}}}\right)\mathbf{j}_{\mathrm{f}}^*(r^* = r_{\mathrm{t}}^*) = \dfrac{1}{\mathrm{Rm}}\left(\dfrac{\sigma_{\mathrm{f}}}{\sigma_{\mathrm{w}}}\right)\left(\dfrac{\partial \mathbf{b}^*(r_{\mathrm{t}}^*)}{\partial r^*}\right) \end{cases} \tag{17}$$

With the current density in the wall calculated from Eqs. (17), its magnetic field density could be found by applying the Biot-Savart law and integrating over the cross-section of the wall as follows:

$$\mathbf{b}_{x\mathrm{w}}^* = \frac{1}{\pi}\left(\frac{e\sigma_{\mathrm{w}}}{g\sigma_{\mathrm{f}}}\right)\left(\frac{\partial b^*(r_{\mathrm{t}})}{\partial r^*}\right)\tan^{-1}\left(\frac{L}{2g}\right)\hat{\mathbf{x}}. \tag{18}$$

The factor $e\sigma_{\mathrm{w}}/g\sigma_{\mathrm{f}}$ is the *conductance ratio*. Thirdly, using the same method of calculation that was applied for the contribution of the wall, the magnetic flux density due to the induced current in the load will be according to equation

$$\mathbf{b}_{x\mathrm{L}}^* = \left(\frac{N_{\mathrm{c}}}{\pi}\right)\left(\frac{g}{L_{\mathrm{B}}}\right)i^*\left(\frac{L_{\mathrm{B}}}{2(g + h_{\mathrm{M}})}\right)\hat{\mathbf{x}}, \tag{19}$$

where N_{c} is the number of turns of the coil. Thus the current in the load depends on the load characteristics as well as on the induced voltage due to the oscillation of the magnetic flux in the coil electrical circuit as the source term. The load circuit configuration, as demonstrated in Fig. 3, includes the inductor L_{C} and its self-resistance r_{C}, the output load modelled with a resistor R_{L} and a correction capacitor C_{c} to adjust the maximum efficiency at the operating frequency. Considering the Lenz law in the coil ($U^* = -N_{\mathrm{C}}S_{\mathrm{i}}^*\mathrm{Rm}(\mathrm{d}b_{x\mathrm{b}}^*/\mathrm{d}t^*)$), the non dimensional equation of the load circuit is

$$-N_{\mathrm{c}}S_{\mathrm{i}}^*\mathrm{Rm}\frac{\mathrm{d}b_{x\mathrm{b}}^*}{dt^*} + \frac{1}{\mathrm{Rm}}(R_{\mathrm{L}} + r_{\mathrm{C}})i^* + \frac{1}{\mathrm{Rm}C_{\mathrm{c}}^*}\int i^*\mathrm{d}t^* = 0. \tag{20}$$

The dimensionless form of of the solution of Eq. (20) yields

$$i^* = \frac{C\mu_0 N_{\mathrm{c}}S_{\mathrm{i}}\omega^2}{g(1 + i(R_{\mathrm{L}} + r_{\mathrm{C}})C_c\omega)}\, b_{x\mathrm{b}}^* = K_{\mathrm{L}}b_{x\mathrm{b}}^*, \tag{21}$$

with K_{L} being a non-dimension constant that includes the load circuit parameters and relates the current in the load with the induced magnetic flux density in the channel. The latter boundary condition is the induced magnetic flux density at

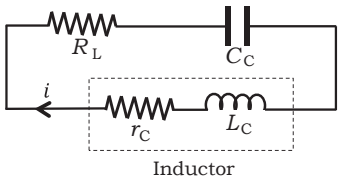

Fig. 3. Load circuit configuration.

Table 4. Non-dimensional parameters applied to the analytical calculation.

Rm	Re_ω	K_{p}	N	K_{L}
0.051	32512	6.22	0.57	$5.68{\times}10^{-4} - i3.51 \times 10^{-3}$

the top of the MHD channel (i.e. $b^*_{x\mathrm{t}} = b^*_x(r^* = r^*_{\mathrm{t}})$). This item could be achieved by applying the Ampere's law once at the bottom and once at the top of the channel, and in both cases to consider the yoke of the MHD generator as a part of the enclosing path. We could obtain the relation between the induced magnetic flux density at the either limits of the channel. The Ampere's law on paths (1) and (2) will lead to

$$\sum h^* l^* = \frac{1}{\mu_0} I^*_{\mathrm{in}}, \tag{22}$$

where h and l are the magnetic field intensity and the length of the path and I_{in} is the current inside the path. This calculation will result in

$$b^*_{x\mathrm{t}} = \frac{1}{2}\left(\left(\frac{\mu_{\mathrm{f}}}{\mu_{\mathrm{i}}}\right)^2\left(2\frac{g}{L_B}\frac{\mu_{\mathrm{i}}}{\mu_{\mathrm{f}}}.\frac{S_{\mathrm{i}}}{S_{\mathrm{e}}} + 1\right) + 1\right) b^*_{x\mathrm{b}}. \tag{23}$$

3. Analytical results and discussion. The system of differential equations (10) could be solved with the boundary conditions mentioned in Eqs. (11), (16), (18) and (19). The non-dimensional parameters applied to the model are presented in Table 4. In this section, the sensitivity of the solution versus different non-dimensional parameters will be analyzed.

Fig. 4 illustrates the time evolution of the velocity profile in the channel. The core has a constant velocity, while in the boundary layer a different behavior is observed that is caused by the viscosity. This effect is very important because it produces a reverse flow (see Fig. 4*f*). This can be explained by the diffusion time of the viscous forces, which introduces a phase shift between the velocity in the core and in the boundary layer of the channel.

The phenomenological explanation of this reverse flow is given below. The typical time of the diffusion of viscosity is

$$T_\nu \approx \frac{d^2}{\nu}, \tag{24}$$

where ν is the kinematic viscosity and d is the depth of the viscous boundary layer. The typical time of the reverse flow oscillations in the core of the channel is

$$T_\omega \approx \frac{1}{\omega}, \tag{25}$$

with ω as the frequency of the oscillations. So the distance from the wall, on which the phase shift between the wall velocity and the core of the channel occurs, can

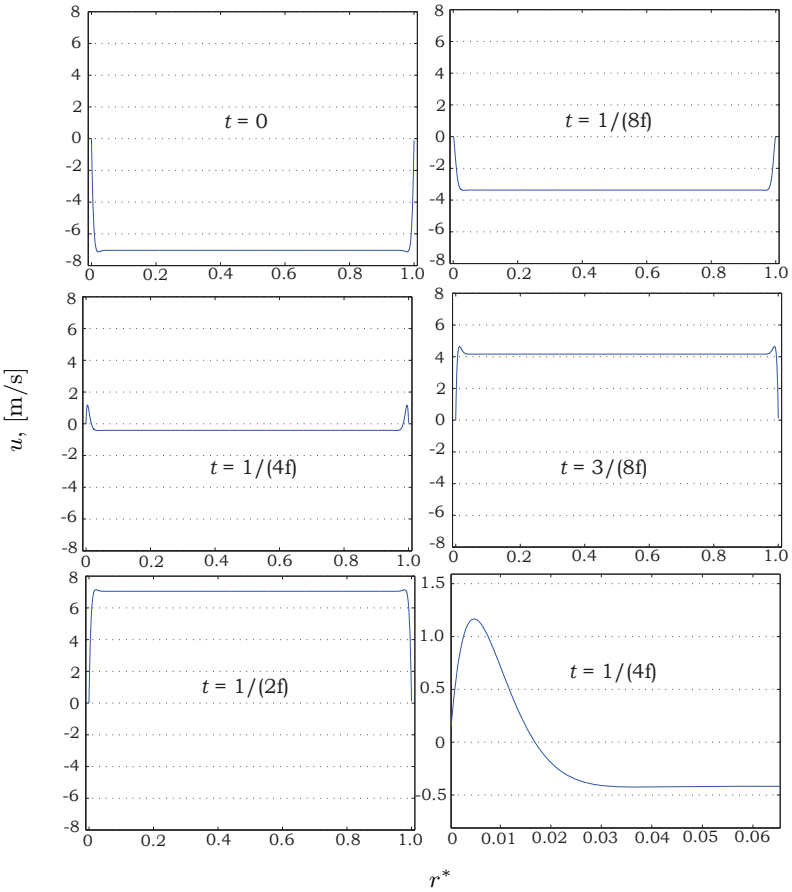

Fig. 4. The velocity profile of liquid sodium inside the MHD channel for six instants according to the parameters mentioned in Table 4. Fig. 4*f* demonstrates a phase shift between the velocity amplitude in the body and in the boundary layer of the channel while changing the velocity direction in the channel.

be estimated from the equality of the two typical times. That gives

$$d \approx \sqrt{\frac{\nu}{\omega}}. \tag{26}$$

Fig. 5a depicts the induced magnetic flux density profile inside the MHD channel. Since the velocity in the core of the channel has a constant value, according to formula (5) for the induced current density inside the MHD channel, **j** is also constant. Then the induced magnetic flux density derivation which is proportional to the current density as

$$j^* = \frac{\partial b_x^*}{\partial r^*} \tag{27}$$

will be also constant. This means a linear behavior of the induced field in the core of the MHD channel that is obvious from Fig. 5. The viscosity effect is visible via the change in b_x^* slope in the boundary layer. This phenomenon could be explained also by the induced current density profile in the channel presented in Fig. 5*b*. According to Eq. (5), the current density in the core of the channel is constant if the velocity and the electric field (E) are also constant, as demonstrated before. But in the boundary layer, as the velocity drops to zero, the electric field

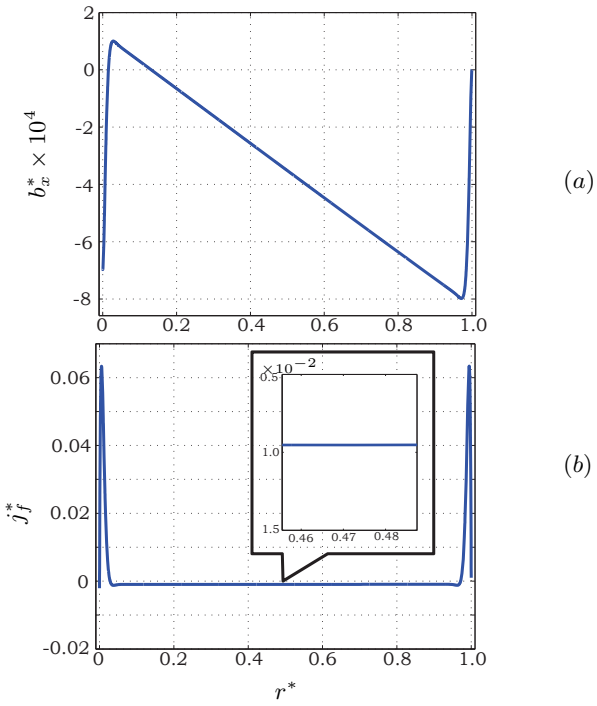

Fig. 5. Dimensionless induced magnetic flux density (a) and induced current density (b) profiles in the MHD channel.

(which is still constant) dominates and changes the sign of the induced current. A consequence of this reversed induced current is that the electromagnetic forces are directed in the flow direction; they are in the same sense as the applied pressure forces. So they are motive forces and contribute to the power transmission when, in the center, the electromagnetic forces act against the flow and then they are resistive. But on the other hand, the very high electric current in the boundary layer induces high Joule losses in such a way that the balance of the reverse flow near the walls is negative.

The efficiency of the MHD generator is calculated as the ratio of the extracted power from the load to the input power into the system. Since a resistive load is used in the load circuit (Fig. 3), the output power is the Ohmic loss in resistance that is calculated as

$$P_{\text{out}}^* = \frac{1}{2} R_{\text{L}}^* I_{\text{max}}^{*2}, \tag{28}$$

where I_{max}^* is the amplitude of the dimensionless current in the load circuit. The input power is the summation of the output power and of all losses in the circuit. Different power losses could be listed as below:

- P_{coil}^*: dimensionless Ohmic power loss in the coil;
- $P_{j\text{f}}^*$: dimensionless Ohmic power loss in the liquid;
- $P_{j\text{w}}^*$: dimensionless Ohmic power loss in the conducting wall;
- P_{fr}^*: dimensionless mechanical friction losses in liquid metal.

The Ohmic loss in the coil is obtained in a similar way as the output power. The fluid Ohmic loss is obtained by a volume integral over the partial Ohmic loss due to the induced current in liquid metal (29), while the Ohmic loss in the

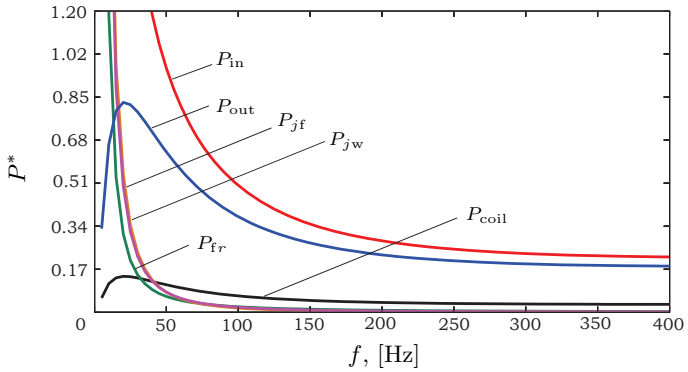

Fig. 6. Different dimensionless power levels of the system versus the operating frequency.

conducting wall is calculated by a volume integral over the partial Ohmic loss due to the induced current in the wall:

$$P^*_{j\rm f} = 2\pi r^*_{ch}\frac{L_{\rm B}}{g}\int_{r^*_{\rm b}}^{r^*_{\rm t}} \bar{j}^{*2}{\rm d}r^*, \tag{29}$$

$$P^*_{j\rm w} = 2\pi r^*_{ch}\frac{\sigma_{\rm f}}{\sigma_{\rm w}}\frac{L_{\rm B}}{g}\int_{r^*_{\rm b}}^{r^*_{\rm t}} j^{*2}_{\rm w}{\rm d}r^*, \tag{30}$$

where the bar denotes the average value over a period of time. Mechanical friction losses that occur due to the viscous effects inside the fluid are calculated from Eq. (3):

$$\begin{aligned} P^*_{r\rm f} = {} & \frac{\mu\omega^2 g^2\mu_{\rm f}^2\sigma_{\rm f}}{TB_0^2}\int_T\int_{V^*_{\rm MHD}} \Re{\rm e}\left\{u^*(t)\right\}\frac{{\rm d}^2\Re{\rm e}\left\{u^*(t)\right\}}{{\rm d}r^{*2}}{\rm d}V_{\rm MHD}{\rm d}t = \\ & \frac{\mu\omega^2 g^2\mu_{\rm f}^2\sigma_{\rm f}}{2B_0^2}\int_{V^*_{\rm MHD}}\left(\Re{\rm e}\left\{|u^*|\right\}\frac{{\rm d}^2\Re{\rm e}\left\{|u^*|\right\}}{{\rm d}r^{*2}}+\Im{\rm m}\left\{|u^*|\right\}\frac{{\rm d}^2\Im{\rm m}\left\{|u^*|\right\}}{{\rm d}r^{*2}}\right){\rm d}V_{\rm MHD}, \end{aligned} \tag{31}$$

where $V^*_{\rm MHD}$ is the dimensionless volume of the MHD channel, $\Re{\rm e}$ and $\Im{\rm m}$ are the real and imaginary values. Then one can derive the efficiency as

$$\eta = \frac{P_{\rm out}}{P_{\rm in}} = \frac{P_{\rm out}}{P_{\rm coil}+P_{j\rm f}+P_{j\rm w}+P_{\rm fr}}. \tag{32}$$

Fig. 6 shows the sensitivity analysis of different power contributions of the system versus the frequency. It could be observed that the viscous loss disappears at higher frequencies. This occurs because the distortion in velocity profile (introduced in Eq. (3) by ${\rm d}^2u^*/{\rm d}r^{*2}$) that is caused by the viscosity will be damped by increasing the frequency. This occurs because the depth of the near wall zone affected by the viscosity decreases when the frequency increases (see Eq. (26)). Then the boundary layer will be limited to a very narrow band beside the either sides of the channel.

Moreover, since the depth of the induced AC magnetic field penetration into a conducting media also decreases when the frequency increases, at higher frequencies the Ohmic losses into the liquid and wall decrease as the load current tends to zero. This, in turn, will reduce the total Ohmic losses and the output power into the function of frequency. So at the high frequency the efficiency tends to

unity, but the output power decreases. This power tends to zero at a very high frequency.

The output power exhibits a maximum value that corresponds to an optimized configuration of the load circuit.

4. Conclusion. This paper describes an analytical approach to study the MHD generator which is in connection with a thermoacoustic engine that applies the fluid oscillation to the MHD channel. The analytical model is based on a system of differential equations, containing the Navier–Stokes equation and the induction equation. The non-dimensionalized differential equations are explained according to the MHD non-dimensional parameters. The solution of the system is obtained by applying the velocity and the induced magnetic field boundary conditions. The results of the different parameters and the sensitivity analysis of the system are presented for a specific situation, as well as a general solution based on the non-dimensional MHD parameters.

REFERENCES

[1] A.A. Castrejn-Pita, G. Huelsz. Heat-to-electricity thermoacoustic-magnetohydrodynamic conversion. *Applied Physics Letters*, vol. 90 (2007), p. 174110.

[2] S.C. Schreppl, I.J. Busch-Vishni. A magnetohydrodynamic underwater acoustic transducer. *J. Acoust. Soc. Am.*, vol. 89 (1991) 2.

[3] A. Alemany, A. Krauze, M. Al Radi. Thermoacoustic–MHD electrical generator. *Energy Procedia*, vol. 6 (2011), pp. 92–100.

[4] J.L. Neuringer. Optimum power generation from a moving plasma. *J. Fluid Mech.,* vol. 7 (1960), pp. 287–301.

[5] S.M. Aithal. Analysis of optimum power extraction in an MHD generator with spatially varying electrical conductivity. *International Journal of Thermal Sciences*, vol. 47 (2008), pp. 1107–1112.

[6] P. Satyamurthy, N. Venkatramani, A.M. Quraishi, A. Mushtaq. Basic design of a prototype liquid metal magnetohydrodynamic power generator for solar and waste heat. *Energy Conversion and Management*, vol. 40 (1999), pp. 913–935.

[7] G. Fabris, E.S. Pierson. The role of interfacial heat and mechanical energy transfer in a liquid-metal MHD generator. *J. Energy Conversion*, vol. 19 (1979), pp. 111–118.

[8] N.S. Dixit, T.K. Thyiagarajan, P. Satyamurthy, N. Venkartramani. Experimental study on the effect of insulating van and interaction parameter on current and voltage in a liquid metal MHD generator. *J. Energy Conversion*, vol. 35 (1994), pp. 643–649.

[9] F. Jousselin, A. Alemany, F. Werkoff, Ph. Marty. MHD induction generator at weak magnetic Reynolds number, Part I. Self excitation criterion and efficiency. *European Journal of Mechanics B/Fluids*, vol. 8 (1989), pp. 23–39.

[10] F. Jousselin, Ph. Marty, A. Alemany, F. Werkoff. MHD induction generator at weak magnetic Reynolds number, Part II. Numerical modelisation and experimental study. *European Journal of Mechanics B/Fluids*, vol. 8 (1989), pp. 327–350.

[11] C. Vogin, A. Alemany. Analysis of the flow in a thermo-acoustic MHD generator with conducting wall. *European Journal of Mechanics B/Fluids*, vol. 26 (2007), pp. 479–493.

[12] S.M.H. Mirhoseini, K. Van Reusel, J. Driesen. Meltpool deformation by magnetic pressure: analytical and experimental approach. *Magnetohydrodynamics*, vol. 51 (2015), no. 1, pp. 105–120.

[13] S.M.H. Mirhoseini, A. Alemany. Analytical Calculation of Thermoacoustic Magnetohydrodynamic (TA-MHD) Generator. *Proc. the 9th International* pamir *Conference on Fundamental and Applied MHD, Thermo Acoustic and Space Technologies* (Riga, Latvia, June 16–20, 2014)

[14] S.M.H. Mirhoseini, K. Van Reusel, J. Driesen. Investigation of Meltpool Deformation by Magnetic Pressure: Analytical and Experimental. *Proc. of the 7th International Scientific Colloquium "Modelling for Electromagnetic Processing" MEP 2014* (Hannover, Germany, September 16–19, 2014).

Received 19.01.2015